

# Volumetric Calculation of Quantization Error in 3-D Vision Systems

Eleni Bohacek, Andrew J. Coates, and David R. Selviah

**Abstract**—This paper investigates how the inherent quantization of camera sensors introduces uncertainty in the calculated position of an observed feature during 3-D mapping. It is typically assumed that pixels and scene features are points, however, a pixel is a two-dimensional area that maps onto multiple points in the scene. This uncertainty region is a bound for quantization error in the calculated point positions. Earlier studies calculated the volume of two intersecting pixel views, approximated as a cuboid, by projecting pyramids and cones from the pixels into the scene. In this paper, we reverse this approach by generating an array of scene points and calculating which scene points are detected by which pixel in each camera. This enables us to map the uncertainty regions for every pixel correspondence for a given camera system in one calculation, without approximating the complex shapes. The dependence of the volumes of the uncertainty regions on camera baseline length, focal length, pixel size, and distance to object, shows that earlier studies overestimated the quantization error by at least a factor of two. For static camera systems the method can also be used to determine volumetric scene geometry without the need to calculate disparity maps.

**Index Terms**—Error analysis, quantization, imaging geometry, ray tracing, 3D/stereo scene analysis, stereo, vision, sensors



## 1 INTRODUCTION

THREE dimensional (3-D) scene reconstruction from multiple views is one of the oldest fields of computer vision and photogrammetry, and it has diverse applications including autonomous vehicle navigation, historical conservation, and industrial tasks such as process inspection and quality assurance [1], [2], [3]. Stereo reconstruction is a process which calculates the position of an object feature in 3-D space by detecting it in two images. This can be summarized in the following steps:

- 1) Geometric calibration determines the intrinsic and extrinsic camera parameters.
- 2) Correspondence matching identifies the pairs of pixels that view the same object.
- 3) Triangulation calculates the 3-D position of the object using disparity in the image plane.

Point clouds (and depth or disparity maps) are the most primitive 3-D data calculated from these processes. Every point in a point cloud has an  $x$ ,  $y$ ,  $z$  value in Euclidean space and a brightness (color or black and white). However, this 3-D information is meaningless if we have not characterized its associated uncertainty, reliability, reproducibility, and errors. The uncertainty in brightness is determined by radiometric factors such as the surface properties and illumination conditions [4], [5]. The uncertainty in position is caused by errors at all three stages of stereo reconstruction, system geometry and image plane quantization.

A lot of research has been carried out into the study of errors generated from calibration [6], [7], [8], [9], [10] and correspondence matching [11], [12], [13], [14], [15],

[16]. There is also a disparate body of research that we summarize as geometrical constraints on error, which is concerned with the fundamental limitations on what a given system of cameras can measure. These factors include intrinsic camera properties, such as the sensor dimensions and focal length, and extrinsic camera properties, such as their baseline distance and angle of focal axis convergence [7], [9], [17]. Another geometrical constraint is the quantization of the image plane into pixels by the camera sensor (such as a CCD or CMOS), which gives rise to errors in point position called quantization error [18], [19].

### 1.1 Image Plane Quantization Error

Many 3-D from stereo algorithms use the disparity in the image planes to calculate 3-D position using triangulation [20]. This assumes that two lines from the perspective center of each camera,  $A$  and  $B$  in figure 1, intersect at the object position in space, denoted by  $X$ . These lines intersect with the image planes at  $w_A$  and  $w_B$ , this is further discussed in section 2.1. By this stage of the calculation, errors in the object position on the image plane have been introduced, which may produce projection lines that do not intersect [21], motivating studies of how to minimize and adjust the errors in the image plane [20], [22]. Furthermore, the quantization of the camera sensor introduces limitations in the spatial resolution of the image plane, which is problematic because triangulation assumes pixels to be points rather than rectangles [19].

If we model a pixel as a rectangle instead of a point, and its projection into space as a pyramid instead of a ray during triangulation, we can calculate the localization error caused by image plane quantization. The intersection of two pyramids gives a polyhedron of six or more sides, which represents an absolute uncertainty bound for the calculated object position, illustrated in fig. 2. This is referred to as an uncertainty region or error volume [18], [19].

- E. Bohacek and D. R. Selviah are with the Department of Electronic and Electrical Engineering, University College London (UCL), WC1E 7JE, United Kingdom.  
E-mail: eleni.bohacek.10@ucl.ac.uk
- A. J. Coates is with the Mullard Space Science Laboratory, University College London.

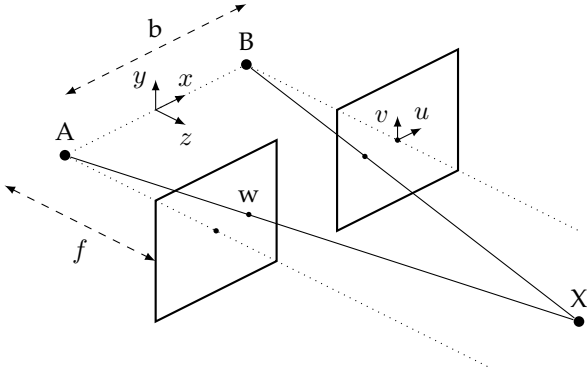


Fig. 1. Perspective projection geometry for two coplanar cameras.

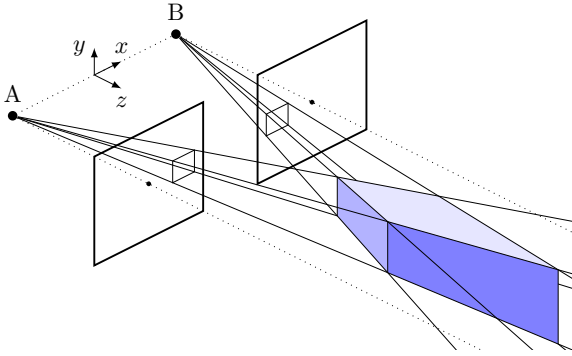


Fig. 2. Perspective projection of pyramids to represent pixel views. The intersection of these pyramids is a polyhedron.

Wu, Sharma and Huang pioneered this approach in 1998, and used the volume of the polyhedron as an error measurement [19]. Limited by computational power at the time, rather than calculating the volume of the polyhedron, they fit the vertices to an ellipsoid using principle component analysis and worked with the ellipsoid volume instead. They also suggested that the ratio of major to minor axis and the direction and size of the major axis gives a quantitative measure of localization error due to quantization.

The idea was picked up again by Fooladgar et al. in 2013, where they applied the idea to circular pixels, which makes the field of view a cone instead of a pyramid [18]. The intersection of two cones is a non-trivial problem that can be solved using a Lagrangian method. They further proposed two analytic solutions that reduce the computational cost by assuming one pixel projection is a cone and the other is four planes, the faces of a pyramid. Due to computational limitations they took the maximum and minimum coordinate values of the polyhedron vertices to approximate this shape as a cuboid. Both the polyhedron volume and the cuboid volume have the same dimensions in  $x$ ,  $y$  and  $z$ , as shown in fig. 3. The volume of the polyhedron (green) will always be less than the cuboid (blue), depending on the nature of the shape this can be a large or a small difference. The ellipsoid volume used in [19] would be fitted to the vertices of the polyhedron.

Both studies present methods to calculate ellipsoid or cuboid approximations of the polyhedral error volume, for one pixel combination at a time. In this paper, we present a method to calculate the true polyhedron volume for all

pixel combinations in a stereo pair. Rather than calculating the complex polyhedral shape of each intersection by projecting pyramids or cones, our method generates a three-dimensional array of gridpoints in the scene and determines which gridpoints are within each intersection. This is the inverse problem of the previous approaches and the discretization of scene space is a technique used in occupancy grid mapping (see section 1.2.2) and volumetric scene reconstruction 1.2.3. Given each camera we calculate which gridpoints are seen by each pixel and perform an intersection of these sets to obtain every uncertainty volume within that space. The method can be used for  $n$  cameras with any rotation or translation between them (provided that their views overlap), but for this study we demonstrate the method using two coplanar camera views. In line with the earlier studies we investigate the effects of camera separation (baseline distance), focal length, pixel size and gridpoint position on the polyhedral and cuboid uncertainty volumes, and compared the latter results with [18].

## 1.2 Related Work

### 1.2.1 Geometric Constraints on Localization Error

Modelling and predicting the accuracy of 3-D from stereo calculations has been a common goal of many studies over the last 40 years. Here we explore a subset of that research, concerning “geometrical constraints on error” as defined in section 1.

One study presents an empirically derived model for the total absolute error in the  $x$ ,  $y$ , and  $z$  coordinates (as defined in fig. 1) of a measured point, whereby the error for each coordinate is a sum of systematic and random components [23]. They predict a similar total absolute error for the  $x$  and  $y$  coordinates and an order of magnitude greater error for the  $z$  coordinate, although by their own admission these estimates are “pessimistically high”. Even if not using this method, stating the error in each Cartesian direction as a confidence interval (for example  $z = 2 \pm 0.1 m$ ) is a typical approach.

An equation of the following form has been used to define the total error of a point  $\varepsilon$ ,

$$\varepsilon = \sqrt{\varepsilon_x^2 + \varepsilon_y^2 + \varepsilon_z^2} \quad (1)$$

whereby  $\varepsilon_x$  represents the variance of the  $x$  coordinate [7] or  $\varepsilon_x$  represents simulated absolute errors of the  $x$  coordinate [6], [9], [24]. Physically this represents the magnitude of the vector connecting the true and measured location of the point. The magnitude of the three components can be very different (see section 5) and this dimensionality information is lost when calculating this quantity, as this effectively this models the uncertainty volume as a sphere.

A model by Yang et al. shows how baseline distance, focal length, and convergence angle separately affect  $\varepsilon$ , and also uses a transfer function to see how they work in combination [9]. Kytö et al. performed an experiment with a multi-level calibration target to examine the effect of baseline distance and focal length on just depth error  $\varepsilon_z$  [17]. Similarly, Ortiz et al. only looked at depth error but varied the resolution setting of their camera [25].

In many papers, half the length of a pixel is assumed to be the quantization error for any point measured by the

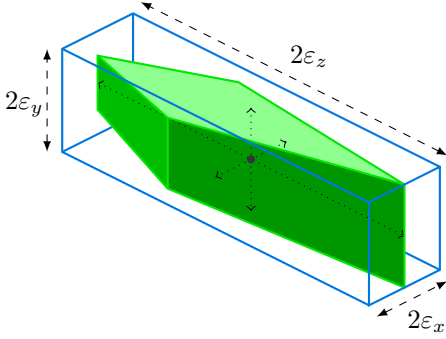


Fig. 3. Quantization uncertainty bounds for a 3-D point (black). The green shape represents the polyhedral volume and the blue lines represent the cuboid volume.

system [7], [26], [27], and this was thought to be dependent on depth but independent of other geometric factors such as camera separation, focal length and position in the other two directions. Wu et al. and Fooladgar et al. demonstrated that quantization error is highly dependent on these factors by modelling the uncertainty volumes (see preceding section) rather than just the total magnitude in (1). Uncertainty volumes have also been used in other studies as a way to communicate the probabilistic nature of calculated 3-D point positions, for example De Cecco et al. generated uncertainty ellipsoids to take into account the uncertainties from calibration and stereo matching [28].

### 1.2.2 Occupancy Grid Mapping

In order to deal with sensor uncertainty, occupancy grid mapping represents the environment in a different way to a point cloud. The continuous space of the scene is discretized into a three-dimensional array and one calculates the probability that each gridpoint is occupied. This volumetric reconstruction method came about in the field of autonomous robot navigation with sonar in mind [29], and starkly contrasted with surface reconstruction methods in robot perception. Occupancy grids can easily integrate noisy sensor data and different sensor modalities, such as LIDAR and photogrammetry, into a single environment map [30]. In addition to modelling objects, the process also models free space and unseen space, which is ideal for applications like path planning and robotic arm manipulation. The accuracy of this technique is dependent on the degree of discretization of the scene space (the resolution of the grid) and the probability model.

Although it has been used with stereo vision and triangulation [31], there has been more work on distance to sensor methods such as disparity maps [32], [33] as these are more computationally efficient for a mobile robot [34].

### 1.2.3 Volumetric Scene Representation

2-D image data has however been used extensively for volumetric scene reconstruction within the field of computer vision. Early attempts focused on segmenting the scene into a foreground and background and intersecting the foreground silhouettes of multiple views. This represents the maximal space occupied by the object, known as the visual hull, and is represented by voxels [35], [36]. One approach to building the visual hull is voxel or space carving,

whereby voxels determined to be outside the visual hull are progressively removed from the initial 3-dimensional grid [37], [38], [39]. Another approach is to additively build the visual hull using constructive solid geometry intersections [40].

Conceptually some of these approaches are similar to the method presented in this paper. Lok describes the visual hull as "the 3-D intersection of all object pixel projection volumes" [41]. The first authors to calculate the pixel viewing a given voxel are Fromhertz et al. in 1994, using the rotation and translation of the object on a rotating stage [42]. Quantization artifacts are a major drawback of volumetric scene reconstruction [40], [43], consequently this framework is the ideal way to measure quantization uncertainty. Our method calculates the visual hull of every pixel combination in a system, and from this it would be possible to determine the visual hull of an object spanning multiple pixels in the images.

## 2 BACKGROUND

### 2.1 Pinhole Camera Model

In keeping with earlier studies, we assume the pin-hole camera model for a low distortion system [44]. Light from a world point at  $\vec{X}$ ,  $(X, Y, Z)$  in world coordinates, passes through the aperture or optic center, and is projected to the image at  $\vec{w}$ ,  $(u, v)$  in image coordinates. In fig. 1, the optic centers are at  $A$  and  $B$  and the image planes have been reflected with respect to the  $XY$  plane at  $z = 0$  so that it does not produce a mirror image with negative coordinates, as is more commonly seen in pinhole camera diagrams [4]. The distance between the cameras or baseline is represented by  $b$ , with the origin of the world coordinates at the midpoint. For these coplanar cameras, the  $x$  and  $y$  axes correspond to the  $u$  and  $v$  directions in image coordinates respectively, and the  $z$  axis is parallel to the optical axes, which corresponds to depth in the scene.  $f$  is the distance from the optic center to the image plane, commonly referred to as the focal length because this refers to the same quantity in the context of lenses. The image plane is assumed to be the same as the sensor plane, and since the image plane is discretized into pixels, the projected world points will be at within  $\pm \frac{1}{2}$  pixel length of the true point [19].

### 2.2 Perspective Projection Model

The transformation from three-dimensional world coordinates to two-dimensional image coordinates is called perspective projection [45]. Three components are required to model the imaging process from the world point  $\vec{X}$  to the pixel  $\vec{w}$ . These are the pixel to image plane conversion,  $\mathbf{C}$ , perspective projection,  $\mathbf{P}$ , and a rigid body transformation,  $\mathbf{R}$ . These are expressed by the following linear matrix operation in homogeneous coordinates:

$$\vec{w} = \mathbf{CPR}\vec{X} \quad (2)$$

$$\begin{bmatrix} su \\ sv \\ s \end{bmatrix} = \begin{bmatrix} k_u & 0 & u_0 \\ 0 & k_v & v_0 \\ 0 & 0 & 1 \end{bmatrix} \begin{bmatrix} f & 0 & 0 & 0 \\ 0 & f & 0 & 0 \\ 0 & 0 & 1 & 0 \end{bmatrix} \begin{bmatrix} r_{11} & r_{12} & r_{13} & T_x \\ r_{21} & r_{22} & r_{23} & T_y \\ r_{31} & r_{32} & r_{33} & T_z \\ 0 & 0 & 0 & 1 \end{bmatrix} \begin{bmatrix} \lambda X \\ \lambda Y \\ \lambda Z \\ 1 \end{bmatrix} \quad (3)$$

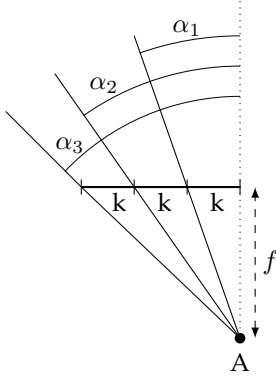


Fig. 4. The angles subtended by each pixel,  $k$ , vary as a function of distance from the optic center (dotted line).

$$\begin{bmatrix} su \\ sv \\ s \end{bmatrix} = \begin{bmatrix} a_u & 0 & u_0 \\ 0 & a_v & v_0 \\ 0 & 0 & 1 \end{bmatrix} \begin{bmatrix} r_{11} & r_{12} & r_{13} & T_x \\ r_{21} & r_{22} & r_{23} & T_y \\ r_{31} & r_{32} & r_{33} & T_z \\ 0 & 0 & 0 & 1 \end{bmatrix} \begin{bmatrix} \lambda X \\ \lambda Y \\ \lambda Z \\ 1 \end{bmatrix} \quad (4)$$

where  $k$  represents the pixel size in either the  $u$  or  $v$  direction,  $u_0$  and  $v_0$  are the position of the optic axis in the image plane,  $f$  is the focal length,  $a_u = fk_u$  and  $a_v = fk_v$  are the image scaling factors, and the ratio  $a_u/a_v$  is the aspect ratio.

In this paper, the optic axis is in the center of the imaging plane, therefore  $a_u = a_v = 1$ , and we assume square pixels so  $k_u = k_v$ . Our pair of cameras are coplanar, meaning their optic axes are parallel so there is no rotational element between them. The world coordinate origin is at the baseline midpoint, therefore the translation  $T$  in  $x$  will be  $T_x = -b/2$  for camera A and  $T_x = b/2$  for camera B, with  $T_y = T_z = 0$ .

### 3 METHODOLOGY

In this section, we summarize how we calculate all the polyhedron uncertainty volumes within a region of space represented by an occupancy grid, which involves simple vector geometry. We then detail how the results can be visualized and queried, such as determining the volume for a specific pair of pixels obtained during correspondence matching. We also present the error metrics used to measure the accuracy of our results.

#### 3.1 Computation of the Intersection Region

We start by defining our region of interest, this can be the entire volume where the two camera views intersect, or a smaller subset of that space. We generate regularly spaced gridpoints filling this volume with cartesian coordinates  $(X, Y, Z)$ . The origin of the coordinate system is at the baseline midpoint. The  $x$ -axis is parallel to the baseline, the  $z$ -axis is depth and the  $y$ -axis is perpendicular to these directions. These grid points can be thought of as the centroids or vertices of cube shaped voxels. The accuracy of this method is highly dependent on the spacing between grid points, so this should be chosen carefully. In section 4.3 we investigate how the grid point spacings affect the calculated volumes for the system we model and a suitable spacing is chosen for the following experiments.

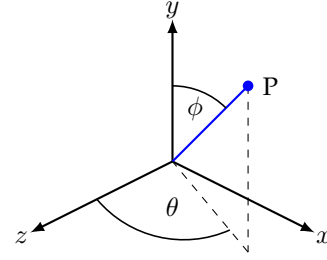


Fig. 5. Spherical coordinates used to define the position of point P.

The following steps, summarized in algorithm 1, determine which gridpoints are in the view of each pixel in one camera. This process is repeated for every other camera or view in the system. We start by specifying the following parameters for the camera:

- Perspective center in world coordinates,  $A$  and  $B$
- Angular field of view in horizontal and vertical directions,  $FOV$
- Focal length,  $f$
- Number of pixels,  $n$
- Pixel size,  $k$

In this study we assume square pixels and equal numbers of detectors in the rows and columns of the sensor. We assume each pixel subtends an angle bounded by planes passing through the camera perspective center,  $A$ , and each pixel border, as shown in fig. 4 in 2-D. The pixel border angles,  $\alpha$ , are calculated using perspective projection, consequently the angle viewed by each pixel decreases with increasing distance from the optic axis.

To calculate the  $\alpha$  angles, we generate a vector containing the  $x$  coordinates of the edges of each pixel  $\vec{x}_k$ , defined by the following sequence  $\langle x \rangle$ :

$$\langle x \rangle = ki, \quad i \in \mathbb{Z}, \quad \frac{-n}{2} \leq i \leq \frac{n}{2} \quad (5)$$

CCDs always have dimensions of powers of 2, so  $n$  will always be even,  $n = 2x, x \in \mathbb{N}$ .  $\alpha$  is then the inverse tangent of  $\langle x \rangle$  divided by the focal length.

$$\vec{\alpha} = \arctan\left(\frac{1}{f} \cdot \vec{x}_k\right) \quad (6)$$

Now that we have the horizontal angles for the pixel edges, we perform the same procedure to determine the vertical angles for the pixel edges,  $\gamma$ . In this work we simulate square pixels therefore  $\gamma = \alpha$ . Next we convert the Cartesian coordinates of each scene grid point,  $P$ , to spherical coordinates with an origin also at the camera center, using the following:

$$\rho = \sqrt{x^2 + y^2 + z^2} \quad (7)$$

$$\phi = \arctan(y/z) \quad (8)$$

$$\theta = \arctan(x/z) \quad (9)$$

whereby  $x, y$  and  $z$  are the cartesian coordinates,  $\rho$  is the distance from the optic center to  $P$ ,  $\phi$  is the elevation, and  $\theta$  is the azimuth relative to the optic axis, shown in fig. 5.

We then determine which pixel view each grid point appears in. The angles in  $\alpha$  are ordered and increasing, therefore, we can determine where  $\theta$  for each grid point fits in to  $\alpha$  by performing a binary search. This returns the index of the element in  $\alpha$  such that if  $\theta$  were inserted into  $\alpha$ , the order of  $\alpha$  would be preserved [46]. This index is  $u$  in the case of  $\theta$  and  $\alpha$ , and  $v$  in the case of  $\phi$  and  $\gamma$ . These are the pixel ID,  $(u, v)$ , for the simulated camera, shown in fig. 1.

We now know for every grid point the cartesian coordinates, spherical coordinates, and pixel ID. These values are stored in a lookup table,  $LUT$ , with the pixel ID as the keys and coordinates as the values. This allows us to look up all the gridpoints seen by a particular pixel, but the keys and values can be readily inverted so that we can look up the pixel viewing each gridpoint. The algorithm is summarized in algorithm 1.

We repeat this process for every other camera in the system, giving us a lookup table for each one, in our case  $LUT_A$  and  $LUT_B$ . By performing an intersection of the gridpoint coordinates in these lookup tables (intersection used in terms of set theory rather than geometry) we obtain both pixel IDs for each gridpoint. This new lookup table,  $LUT_{AB}$ , has the pixel IDs of both cameras as the key,  $[(u_A, v_A), (u_B, v_B)]$ , and all the gridpoints within that intersection as the values. The algorithm steps are described in algorithm 2. If there are three or more views in the system you repeat algorithm 2 with  $LUT_{AB}$  and  $LUT_C$  and so on.

$LUT_{AB}$  contains all the information needed to determine which pixels in cameras  $A$  and  $B$  see any scene point, and conversely which scene points are in the uncertainty volume of any pixel combination.

---

#### Algorithm 1: Gridpoints in view of one camera

---

**Input:**  $R$  = region of interest,  $s$  = gridpoint spacing, camera parameters  $[A, f, n, k]$

```

G = GenerateOccupancyGrid(R, s)
A = new array of length i
for x in ⟨x⟩, where ⟨x_i⟩ is defined in equation 5 do
  compute α using equation 6
  A[i] = α
S = new 3-D array with dimensions G
for x, y, z point in G do
  compute ρ, θ, φ using equations 7, 8, and 9
  S[x, y, z] = ρ, θ, φ
U = new 3-D array with dimensions G
V = new 3-D array with dimensions G
for ρ, θ, φ in S with index x, y, z: do
  U[x, y, z] = FindBinarySearch(A, θ)
  V[x, y, z] = FindBinarySearch(A, φ)
LUT = new lookup table
for x, y, z in G do
  u = U[x, y, z]
  v = V[x, y, z]
  add point P(x, y, z) to current list in R[u, v]

```

**Output:**  $LUT$

---

#### Algorithm 2: Gridpoints in view of 2 or more cameras

---

**Input:**  $LUT_A, LUT_B$   
 $LUT_{AB}$  = new lookup table

```

for u_A, v_A in LUT_A: do
  for u_B, v_B in LUT_B: do
    points_A = LUT_A[u_A, v_A]
    points_B = LUT_B[u_B, v_B]
    intersection = points_A ∩ points_B
    if intersection: then
      intersections[u_A, v_A, u_B, v_B] = intersection

```

**Output:**  $LUT_{AB}$

---

### 3.2 Uncertainty Region Representation

The lookup table made in algorithm 2 can be queried to characterize and plot the uncertainty volumes for cameras  $A$  and  $B$ . The polyhedron volume is obtained by counting the number of points,  $p$ , in each intersection and converting this to a volume in meters cubed using the spacing between grid points,  $g$ :

$$V = g^3 p \quad (10)$$

The cuboid uncertainty volume and its dimensions offer an approximate shape of this region as shown in fig. 3. The cuboid volume is calculated by querying the minimum and maximum coordinate values in an intersection, calculating the  $x$ ,  $y$ , and  $z$  dimensions and multiplying these together. It is possible to examine how the three components contribute to the volume as we vary parameters such as distance from the camera, however the usefulness of this is limited by the degree to which the major and minor axes of the polyhedron align with the cartesian axes.

### 3.3 Error Metrics

To test the validity of our approach we compare our results with those of previous authors in terms of Root Mean Squared (RMS) error:

$$RMS = \sqrt{\frac{\sum_{n=1}^N (p - o)^2}{N}} \quad (11)$$

where  $p$  is the predicted value,  $o$  is the observed value and  $N$  is the number of measurements. For our calculations the predicted values are the cuboid volumes obtained by [18] and the observed values are the cuboid volumes obtained using our method. We want to express the error as a percentage, so rather than use the Mean Absolute Percentage Error (MAPE) [47], which imposes a heavier penalty when  $o < p$ , we use a logarithm of the accuracy ratio,  $p/o$ . This outperforms MAPE when the error grows as a function of a variable [48], which is the case for all our observations. We calculate the Median Symmetric Accuracy (MSA) [49], given by the following:

$$MSA = 100((e^{M|\log_e(p/o)|}) - 1) \quad (12)$$

where  $M$  represents the median function of all values of  $\log_e(p/o)$ .

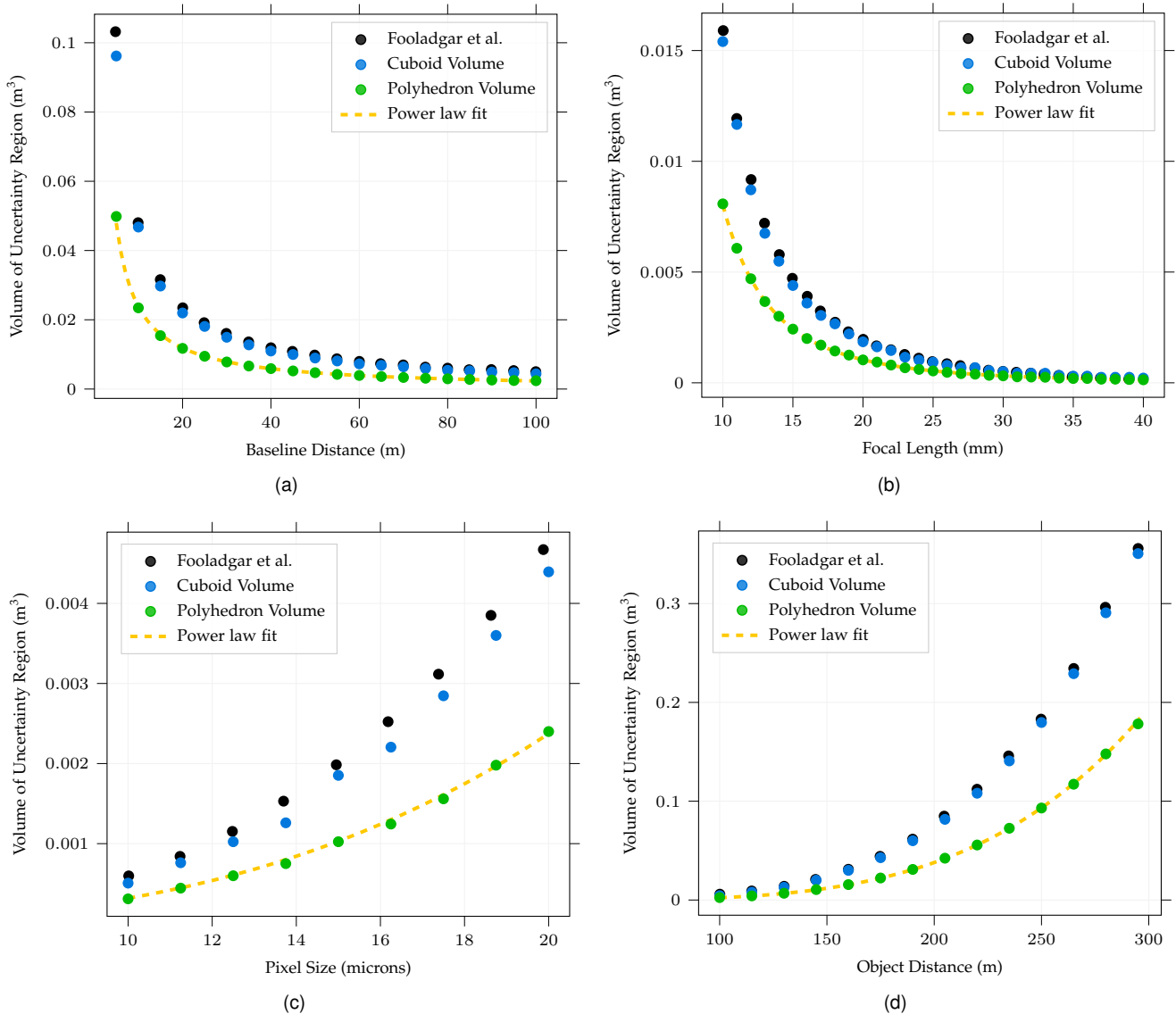


Fig. 6. Volume of uncertainty region versus (a) baseline distance, (b) focal length, (c) pixel size, (d) object distance in the  $z$  direction.

## 4 RESULTS

We present a series of experiments to compare the uncertainty regions calculated using this method with those obtained by earlier studies [18], [19]. Fooladgar et al. showed that the pyramids intersection method used by Wu et al., produced error measures “almost equal” to their cone intersection method. We ran our simulation at “a sufficiently high resolution”, discussed in section 4.3, and calculated the polyhedron error volumes and the cuboid error volumes. We present these two measures alongside those obtained by [18], and we compare our cuboid volumes with their cuboid volumes in terms of Root Mean Square Error (RMSE) and Median Symmetric Accuracy (MSA), shown in table 1. Point for point comparison was not possible as their original data was unavailable so the process of extracting it from the figures introduced a precision error in their results. Our cuboid volumes are consistently lower than theirs because we quantize our scene.

For each experiment, unless the parameter is being var-

ied, the baseline is 100 m, the focal length 15 mm, the pixel size 20  $\mu\text{m}$ , as these were used in the earlier study [18]. The uncertainty volume for an object 100 m away from the cameras was measured each time, except for the object distance experiment where this was increased up to 300 m. The vertical axes for fig 6 show the volume of the uncertainty region in meters cubed, and the horizontal axis the variable of each experiment: baseline, focal length, pixel size, object distance,  $z$ . The gridpoint spacing used to find the cuboid volume and polyhedron volume is 3 per cm, this is further discussed in section 4.3.

### 4.1 Error due to system parameters

Figure 6a shows the effect of baseline length, or camera separation, on uncertainty volume. The decrease in polyhedron volume with increasing baseline distance follows a power law of  $V = 0.2427b^{-1.008}$ , where  $V$  is the volume of the uncertainty region and  $b$  is the baseline distance. Earlier authors reported a similar trend and the results of

TABLE 1

Root mean squared Error (RMSE) and median symmetric accuracy (MSA) of cuboid volumes obtained using our method compared with cuboid volumes obtained by Fooladgar et al.

	Baseline	Focal Length	Pixel Size	Object Distance
RMSE (m <sup>3</sup> )	0.001808	0.000196	0.00022	0.00343
MSA (%)	7.58	3.07	10.47	2.30

[18] are plotted alongside ours for comparison. They attributed the decrease in uncertainty volume with increasing baseline distance to the viewing pixel being further from the sensor center. As the pixel viewing angles decrease the pyramid projections narrow, resulting in smaller intersection volumes, and our findings confirm this. For smaller baselines, the difference between polyhedron volume and cuboid volume is at its largest, and for larger baselines the difference is less marked. The cuboid volume calculation overestimates the localization error by almost two times at 5 m baseline, therefore for smaller baselines the polyhedron volume model would be more suitable.

Figure 6b shows the effect of focal length on error volume. The longer the focal length, the narrower the pyramid so the pyramid intersections are smaller in these cases. The decrease in polyhedron volume also follows a power law of  $V = 7.1298f^{-2.948}$ , and the difference between the two models of error volume is greatest for smaller focal lengths. Figure 6c shows the effect of pixel size on error volume. The increase in polyhedron volume as a function of pixel size can be described with the following power law,  $V = 4 \times 10^{-7}k^{2.9253}$ . The larger the pixel, the wider the pyramid cross section, so the uncertainty volume increases with increasing pixel size.

#### 4.2 Error due to scene point position

Figure 6d shows the effect of object distance or increasing depth,  $z$ , on the error volume. The point to be imaged is 100 m away from the baseline midpoint (0, 0, 100), and the  $z$  value is increased up to 300 m. The uncertainty volume increase with object distance follows a power law of  $V = 2 \times 10^{-11}z^{4.0321}$ . The further away the object, the closer to the center of the sensor it is detected, and the wider the viewing pyramids, hence the larger the intersection volume.

We now look beyond the  $z$  axis to measure uncertainty volumes at different  $x$  and  $y$  positions within a plane perpendicular to this axis. Fig. 7 shows the effect of the  $x$  and  $y$  coordinate on the cuboid error volume. At  $z = 100$  m, a plane of scene points from -100 m to +100 m in  $x$  and  $y$  was generated, and the error volume for each point in this plane was calculated. In the  $x$  direction the uncertainty volumes are lowest at the CCD center and increase as we move left or right in the plane. The cameras are situated at (50, 0, 0) and (-50, 0, 0) in m, and we observe a smaller increase in uncertainty volume for scene points beyond these  $x$  values. The error volume does not change with variation in the  $y$  direction for points within  $\pm 50$  m in  $y$  position but it increases beyond these values. The extent of the same simulations in [18] and [19] was  $\pm 50$  m in  $x$  and  $y$

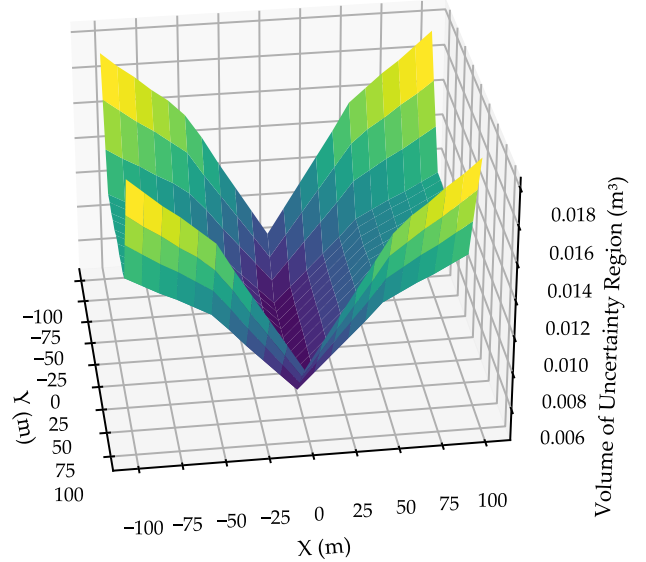


Fig. 7. Volume of cuboid uncertainty region versus object positions within the  $XY$  plane at  $z = 100$  m.

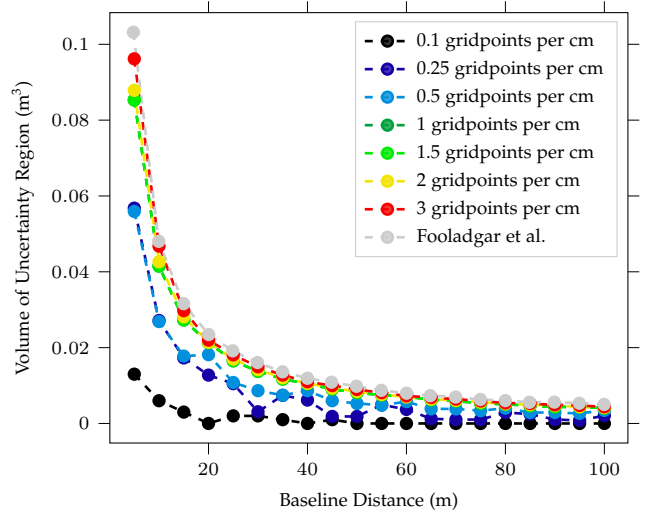


Fig. 8. Volume of cuboid uncertainty region versus baseline distance at different gridpoint spacings.

rather than  $\pm 100$  m. Our results closely match theirs for the same region and we show the trends in uncertainty volumes change beyond this region. We build on earlier studies by also examining how the uncertainty volumes change as a function of position in the other two perpendicular planes,  $XZ$  and  $YZ$ .

Fig. 9 shows the cuboid and polyhedron uncertainty volumes as a function of scene point position within three perpendicular planes that meet at (0, 0, 100). The first of the three plots in fig 9a shows the same data as fig. 7, displayed as a 2-D image. The uncertainty volumes of points within the other two perpendicular planes of the same dimensions are also shown, colorized to the same scale. The variations in uncertainty volumes within the  $XY$  planes in fig. 7 are dwarfed by changes in the  $XZ$  and  $YZ$  planes over the same distances. Fig 9b displays the same plots using the polyhedron volume instead of the box volume

approximation. The colorbar shows that the scale of all these volumes is much smaller. The variation in the  $XY$  plane the previous authors reported is only present when using the cuboid volume approximation. For the  $XZ$  plane, both volumes increase with  $Z$ , and the polyhedron volume is a factor of 4 smaller than the cuboid volume. For the  $YZ$  plane both models show an increase in uncertainty volume with  $Z$  but there is an added  $y$  component in cuboid volume approximation that is not apparent in the polyhedron model.

### 4.3 Grid Point Spacing

The choice of how densely to generate the occupancy grid points strongly affects the calculated volume and the computation time. Here we perform the baseline experiment from the previous section with different grid point spacings ranging from 0.1 per cm to 3 per cm. Figure 8 shows how as the number of scene points per cm is increased, the closer the results fit to the calculations by [18] for the cuboid volume. The authors do not quantize their scene as we do in this method, so our cuboid volumes will never totally align but 3 points every cm at these baseline distances gives a visually close approximation and a total RMS error of uncertainty volumes of our cuboid model compared with the Fooladgar et al. model is  $0.001808 m^3$ , shown in table 1. The comparison of our experiment results with theirs in terms of median symmetric accuracy shows that our inverse method produces similar results to their method. The same inverse method is used to calculate the polyhedron volume, so this suggests our polyhedron volumes are accurate. We use 3 grid points per cm for the experiments in this study unless stated otherwise.

## 5 DISCUSSION

The cuboid volume always overestimates the localization error when compared to the polygon volume, which is unsurprising given the visual representation in figures 2 and 3. In all four experiments, we show this difference increases at larger uncertainty volumes. In all cases, the volumes increase when the size of the pyramids projecting from each pixel increases. This happens at larger pixel sizes, because this increases the pyramid cross section, and smaller focal lengths, which affects the distance between the pyramid apex and the pixels. The volumes also increase in size when the detecting pixel is closer to the center of the image plane. Even though all pixels are the same size and regularly distributed, perspective projection means that the outer pixels subtend smaller angles than those in the center. Larger baselines and smaller distances from the camera give lower localization error because in coplanar stereo cameras the scene point will be detected by pixels further away from the image center.

We might conclude that in a real-world scenario when taking stereo images of an object to make an accurate 3-D model, that the cameras should be aimed to detect the object at the edges rather than the center of the image plane, in order to minimize quantization uncertainty. However, we should also consider that lens distortion is at its greatest at the edges of the image, and at its minimum at the image

center. Lens distortion is more widely considered as a cause of localization error and has been studied extensively in this field. This quantization error model could be combined with lens distortion models in the future to yield more comprehensive localization error predictions for a system.

Previous authors reported variations in uncertainty volume as a function of scene point distance in  $x$ , however, after recreating these results with the cuboid volume model (figure 9a), we show that there is no such trend in the polyhedron model (figure 4.2). We conclude that this trend is an artefact caused by the cuboid approximation. Our results show that only depth,  $z$ , affects the volume of the uncertainty region. A demonstration of the limitations of the cuboid model is shown in fig. 10, which shows voxel plots of two example intersections from the  $XY$  plane in fig. 7. The uncertainty volume in fig. 10a, from the center of the  $XY$  plane, contains 2548 gridpoints, which is converted to a polyhedron volume of  $0.002548 m^3$  and a cuboid volume of  $0.0042 m^3$  using (10). The uncertainty volume in fig.10b, from a corner of the  $XY$  plane, contains 2362 gridpoints, equal to a polyhedron volume of  $0.002362 m^3$  and a cuboid volume of  $0.015 m^3$ . The nature of the two shapes means that despite having similar polyhedron volumes their cuboid volumes are different by an order of magnitude. Intersections at the center of the  $XY$  plane are more closely aligned with the coordinate system axes and the further away from the center the intersections are, the more oblique they become. This means that calculating the cuboid volume from the maxima and minima in gridpoint coordinates can yield a poor fit and result in significant overestimation of uncertainty due to quantization.

## 6 CONCLUSION

Quantization error is not usually factored into error predictions alongside errors from stereo matching and calibration. Wu et al. and Fooladgar et al. modelled quantization error by projecting pyramids or cones into space to calculate the intersection region for a pair of pixels, approximated as an ellipsoid or cuboid. They showed that quantization can introduce significant uncertainties in object feature mapping, however, under the computational restrictions of the time, it was only possible to calculate it for one pair of matched pixels. Our method applies their principle in reverse by quantizing the scene and calculating which pixels see each scene point. This method has the advantage of yielding every possible quantization region for every potential correspondence in the system, for two or more camera views. Furthermore rather than calculating a cuboid approximation of the uncertainty volumes, we calculate the volume of the uncertainty polyhedron itself. We confirmed earlier author's models, and show the cuboid approximation to overestimate the uncertainty volume by at least a factor of two. We present our method as a way to make quantization errors more readily calculable and more precise as they do not need to be approximated.

The advantage of this calculation is that it only needs to be performed once to determine all possible quantization errors for a camera system. Then for example, at the correspondence matching stage of 3-D from stereo, the polyhedral uncertainty volume or cuboid volume dimensions



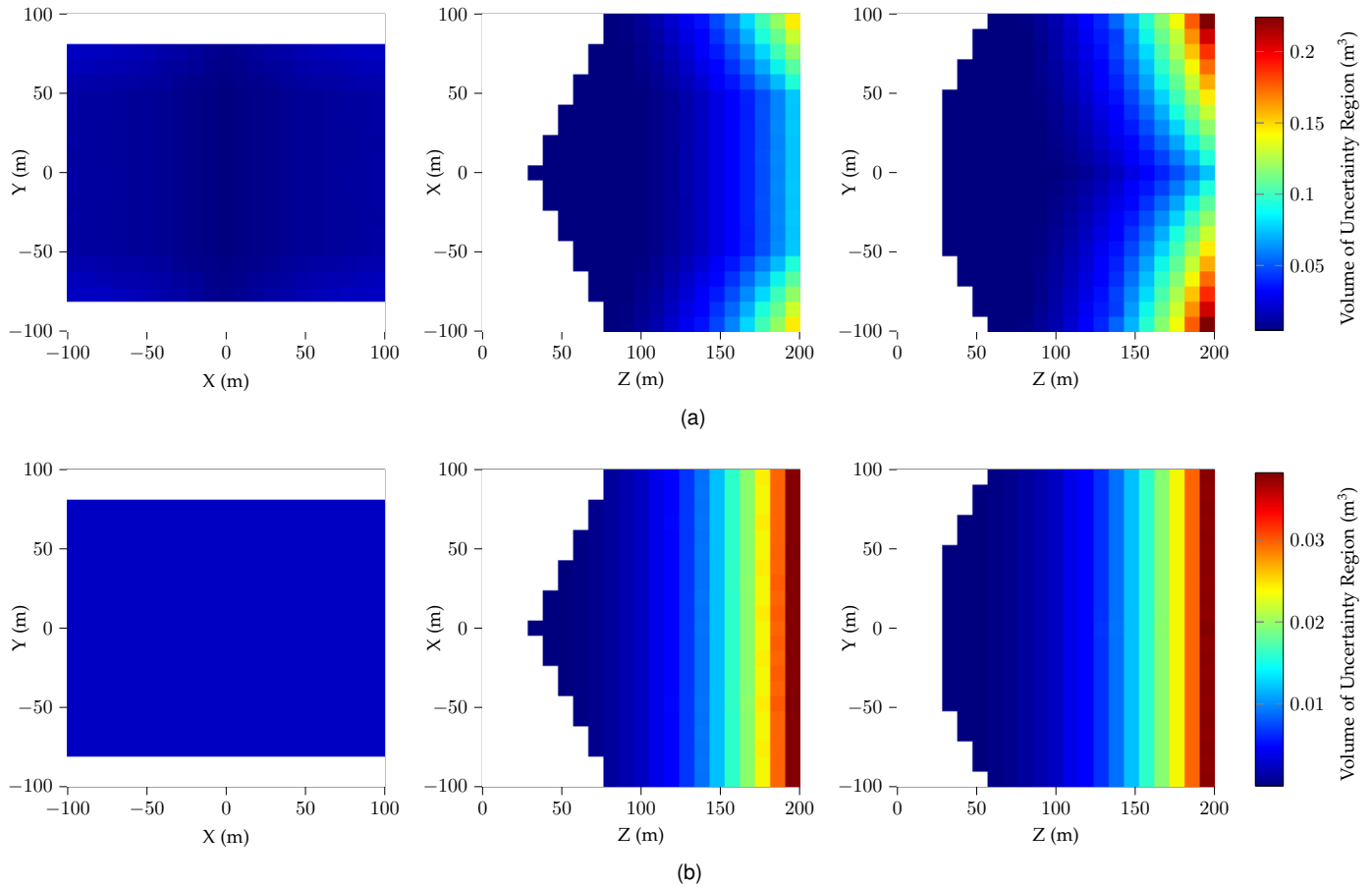


Fig. 9. Volume of cuboid (a) and polyhedron (b) uncertainty region versus object positions within XY plane (left), XZ plane (middle), YZ plane (right)

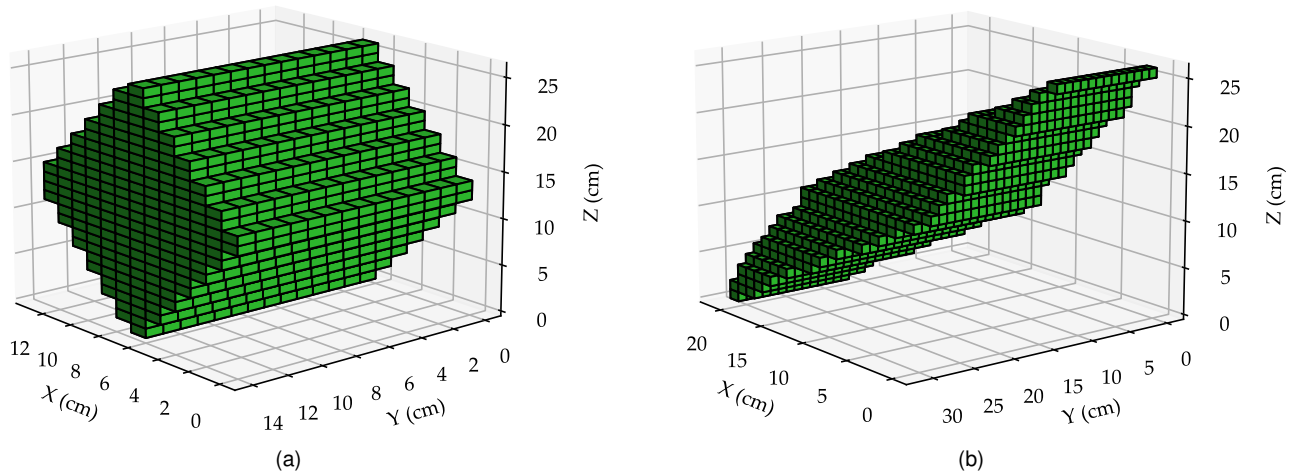


Fig. 10. Voxel plot of two intersections from fig. 7. Plot (a) shows an intersection from the center of the plane at  $x = 0$  m,  $y = 0$  m, Plot (b) shows an intersection from the corner at  $x = -80$  m,  $y = -80$  m. For visual clarity the gridpoints were generated at 1 per cm.

can be queried and saved for each set of matched pixels. Furthermore the triangulation stage is no longer necessary because the object point locations are already known for each pixel correspondence. This has potential applications in mobile robot navigation, as most occupancy grid mapping methods that use camera inputs need to generate disparity maps. Using our method, a robot with multiple cameras

would only need to store and query a look up table to determine scene geometry. Our method also calculates the visual hull on a pixel by pixel basis, so could also be used to construct visual hulls of larger objects spanning. A limitation of this method is that it assumes a static camera system, such as a stereo pair of cameras on a robot. As soon as the spacings of the cameras change, such as a camera

moving through a scene, a new look up table has to be calculated.

Another application of precisely calculated error bounds is in visualization. If we choose to represent the scene as a point cloud rather than an occupancy grid, we can plot the intersection polygons instead of points. Rather than needing to quote a positional error figure for each point, the localization uncertainty is implicit in the shape, making this easier for a human to interpret.

## REFERENCES

- [1] T. Van Damme, "Computer Vision Photogrammetry for underwater archaeological site recording in a low-visibility environment," *ISPRS - International Archives of the Photogrammetry, Remote Sensing and Spatial Information Sciences*, vol. XL-5/W5, pp. 231–238, Apr. 2015.
- [2] N. Yastikli, "Documentation of cultural heritage using digital photogrammetry and laser scanning," *Journal of Cultural Heritage*, vol. 8, no. 4, pp. 423–427, Sep. 2007. [Online]. Available: <https://linkinghub.elsevier.com/retrieve/pii/S1296207407001082>
- [3] K. Khoshelham and S. O. Elberink, "Accuracy and Resolution of Kinect Depth Data for Indoor Mapping Applications," *Sensors*, vol. 12, no. 2, pp. 1437–1454, Feb. 2012. [Online]. Available: <http://www.mdpi.com/1424-8220/12/2/1437>
- [4] M. Sonka, V. Hlavac, and R. Boyle, *Image processing, analysis, and machine vision*, third edition ed. Cengage Learning, 2014.
- [5] G. Kamberova and R. Bajcsy, "Sensor errors and the uncertainties in stereo reconstruction," *Empirical Evaluation Techniques in Computer Vision*, pp. 96–116, 1998.
- [6] Y. Xu, Y. Zhao, F. Wu, and K. Yang, "Error analysis of calibration parameters estimation for binocular stereo vision system," in *2013 IEEE International Conference on Imaging Systems and Techniques (IST)*. IEEE, 2013, pp. 317–320.
- [7] K. Schreive, "How accurate can a stereovision measurement be?" in *15th International Workshop on Research and Education in Mechatronics (REM)*. IEEE, 2014, pp. 1–7.
- [8] G. Di Leo and A. Paolillo, "Uncertainty evaluation of camera model parameters," in *2011 IEEE International Instrumentation and Measurement Technology Conference*. IEEE, 2011, pp. 1–6.
- [9] L. Yang, B. Wang, R. Zhang, H. Zhou, and R. Wang, "Analysis on location accuracy for the binocular stereo vision system," *IEEE Photonics Journal*, vol. 10, no. 1, pp. 1–16, 2017.
- [10] J. Shawash and D. R. Selviah, "Real-Time Nonlinear Parameter Estimation Using the Levenberg–Marquardt Algorithm on Field Programmable Gate Arrays," *IEEE Transactions on Industrial Electronics*, vol. 60, no. 1, pp. 170–176, Jan. 2013. [Online]. Available: <http://ieeexplore.ieee.org/document/6129410/>
- [11] C. J. Ng and B. Farell, "Solving the stereo correspondence problem with false matches," *PLOS ONE*, vol. 14, no. 7, p. e0219052, 2019, publisher: Public Library of Science (PLOS). [Online]. Available: <https://dx.doi.org/10.1371/journal.pone.0219052>
- [12] J. Liu, C. Li, F. Mei, and Z. Wang, "3D entity-based stereo matching with ground control points and joint second-order smoothness prior," *The Visual Computer*, vol. 31, no. 9, pp. 1253–1269, 2015, publisher: Springer Science and Business Media LLC. [Online]. Available: <https://dx.doi.org/10.1007/s00371-014-1009-3>
- [13] J. Ma, J. Zhao, J. Tian, A. L. Yuille, and Z. Tu, "Robust Point Matching via Vector Field Consensus," *IEEE Transactions on Image Processing*, vol. 23, no. 4, pp. 1706–1721, 2014, publisher: Institute of Electrical and Electronics Engineers (IEEE). [Online]. Available: <https://dx.doi.org/10.1109/TIP.2014.2307478>
- [14] D. Scharstein, R. Szeliski, and R. Zabih, "A taxonomy and evaluation of dense two-frame stereo correspondence algorithms." *IEEE Comput. Soc*, 2001. [Online]. Available: <https://dx.doi.org/10.1109/smbv.2001.988771>
- [15] Z. Li and D. Selviah, "Comparison of image alignment algorithms," London, 2011.
- [16] D. Marr and T. Poggio, "Cooperative computation of stereo disparity," *Science*, vol. 194, no. 4262, pp. 283–287, 1976, publisher: American Association for the Advancement of Science (AAAS). [Online]. Available: <https://dx.doi.org/10.1126/science.968482>
- [17] M. Kytö, M. Nuutinen, and P. Oittinen, "Method for measuring stereo camera depth accuracy based on stereoscopic vision," in *Three-Dimensional Imaging, Interaction, and Measurement*, vol. 7864. International Society for Optics and Photonics, 2011, p. 78640I.
- [18] F. Fooladgar, S. Samavi, S. M. R. Sorousmehr, and S. Shirani, "Geometrical Analysis of Localization Error in Stereo Vision Systems," *IEEE Sensors Journal*, vol. 13, no. 11, pp. 4236–4246, Nov. 2013.
- [19] J. J. Wu, R. Sharma, and T. S. Huang, "Analysis of uncertainty bounds due to quantization for three-dimensional position estimation using multiple cameras," *Optical Engineering*, vol. 37, Jan. 1998. [Online]. Available: <http://adsabs.harvard.edu/abs/1998OptEn..37..280W>
- [20] R. I. Hartley and P. Sturm, "Triangulation," *Computer vision and image understanding*, vol. 68, no. 2, pp. 146–157, 1997.
- [21] S. Wenhart, J. Denzler, and H. Niemann, "On minimizing errors in 3D reconstruction for stereo camera systems," *Pattern Recognition and Image Analysis*, vol. 17, no. 2, pp. 337–348, Jun. 2007. [Online]. Available: <https://doi.org/10.1134/S1054661807020228>
- [22] M. Zhang, L. Qi, G. Cui, and M. Yu, "A Triangulation Method in 3D Reconstruction from Image Sequences," in *2009 Second International Conference on Intelligent Networks and Intelligent Systems*. Tianjian, China: IEEE, Nov. 2009, pp. 306–308. [Online]. Available: <http://ieeexplore.ieee.org/document/5365864/>
- [23] W. Sankowski, M. Włodarczyk, D. Kacperski, and K. Grabowski, "Estimation of measurement uncertainty in stereo vision system," *Image and Vision Computing*, vol. 61, pp. 70–81, 2017.
- [24] J. Rodríguez-Quinonez, O. Sergiyenko, W. Flores-Fuentes, M. Rivas-lopez, D. Hernandez-Balbuena, R. Rascón, and P. Mercorelli, "Improve a 3D distance measurement accuracy in stereo vision systems using optimization methods' approach," *Opto-Electronics Review*, vol. 25, no. 1, pp. 24–32, May 2017. [Online]. Available: <https://linkinghub.elsevier.com/retrieve/pii/S1230340217300100>
- [25] L. E. Ortiz, V. E. Cabrera, and L. M. G. Goncalves, "Depth Data Error Modeling of the ZED 3D Vision Sensor from Stereolabs," *ELCVIA Electronic Letters on Computer Vision and Image Analysis*, vol. 17, no. 1, p. 1, Jun. 2018. [Online]. Available: <https://elcvia.cvc.uab.es/article/view/v17-n1-ortiz>
- [26] C. Chang and S. Chatterjee, "Quantization error analysis in stereo vision," in [1992] *Conference Record of the Twenty-Sixth Asilomar Conference on Signals, Systems Computers*, Oct. 1992, pp. 1037–1041 vol.2, ISSN: 1058-6393.
- [27] J. Rodriguez and J. Aggarwal, "Stochastic analysis of stereo quantization error," *IEEE Transactions on Pattern Analysis and Machine Intelligence*, vol. 12, no. 5, pp. 467–470, May 1990. [Online]. Available: <http://ieeexplore.ieee.org/document/55106/>
- [28] M. De Cecco, L. Baglivo, G. Parzianello, M. Lunardelli, F. Setti, and M. Pertile, "Uncertainty analysis for multi-stereo 3d shape estimation." *IEEE*, 2009. [Online]. Available: <https://dx.doi.org/10.1109/AMUEM.2009.5207608>
- [29] A. Elfes, "Using occupancy grids for mobile robot perception and navigation," *Computer*, vol. 22, no. 6, pp. 46–57, 1989, publisher: Institute of Electrical and Electronics Engineers (IEEE). [Online]. Available: <https://dx.doi.org/10.1109/2.30720>
- [30] K. Pirker, M. Ruther, H. Bischof, and G. Schweighofer, "Fast and accurate environment modeling using three-dimensional occupancy grids," in *2011 IEEE International Conference on Computer Vision Workshops (ICCV Workshops)*. Barcelona, Spain: IEEE, Nov. 2011, pp. 1134–1140. [Online]. Available: <http://ieeexplore.ieee.org/document/6130377/>
- [31] H. P. Moravec, "Robot Spatial Perception by Stereoscopic Vision and 3D Evidence Grids," *The Robotics Institute, Carnegie Mellon University, Tech. Rep.*, 1996.
- [32] H. Lategahn, W. Derendarz, T. Graf, B. Kitt, and J. Effertz, "Occupancy grid computation from dense stereo and sparse structure and motion points for automotive applications." *IEEE*, 2010. [Online]. Available: <https://dx.doi.org/10.1109/ivs.2010.5548078>
- [33] F. Andert, "Drawing stereo disparity images into occupancy grids: Measurement model and fast implementation," in *2009 IEEE/RSJ International Conference on Intelligent Robots and Systems*. St. Louis, MO, USA: IEEE, Oct. 2009, pp. 5191–5197. [Online]. Available: <http://ieeexplore.ieee.org/document/5354638/>
- [34] M. Perrollaz, J.-D. Yoder, A. Negre, A. Spalanzani, and C. Laugier, "A Visibility-Based Approach for Occupancy Grid Computation in Disparity Space," *IEEE Transactions on Intelligent Transportation Systems*, vol. 13, no. 3, pp. 1383–1393, 2012, publisher: Institute

of Electrical and Electronics Engineers (IEEE). [Online]. Available: <https://dx.doi.org/10.1109/tits.2012.2188393>

- [35] W. N. Martin and J. K. Aggarwal, "Volumetric Descriptions of Objects from Multiple Views," *IEEE Transactions on Pattern Analysis and Machine Intelligence*, vol. PAMI-5, no. 2, pp. 150–158, Mar. 1983. [Online]. Available: <http://ieeexplore.ieee.org/document/4767367/>
- [36] A. Laurentini, "The Visual Hull Concept for Silhouette-Based Image Understanding," *IEEE Transactions on Pattern Analysis and Machine Intelligence*, vol. 16, no. 2, pp. 150–162, Feb. 1994. [Online]. Available: <https://doi.org/10.1109/34.273735>
- [37] P. Eisert, E. Steinbach, and B. Girod, "Automatic Reconstruction of Stationary 3-D Objects from Multiple Uncalibrated Camera Views," *Ieee Transactions on Circuits and Systems for Video Technology: Special Issue on 3d Video Technology*, vol. 10, pp. 261–277, 2000.
- [38] K. N. Kutulakos and S. M. Seitz, "A Theory of Shape by Space Carving," *International Journal of Computer Vision*, vol. 38, pp. 307–314, 1998.
- [39] C. Theobalt, M. A. Magnor, P. Schüler, and H.-P. Seidel, "Combining 2d feature tracking and volume reconstruction for online video-based human motion capture," *International Journal of Image and Graphics*, vol. 04, no. 04, pp. 563–583, Oct. 2004, publisher: World Scientific Publishing Co. [Online]. Available: <https://www.worldscientific.com/doi/abs/10.1142/S0219467804001543>
- [40] W. Matusik, C. Buehler, R. Raskar, S. J. Gortler, and L. McMillan, "Image-based visual hulls," in *Proceedings of the 27th annual conference on Computer graphics and interactive techniques*, ser. SIGGRAPH '00. USA: ACM Press/Addison-Wesley Publishing Co., Jul. 2000, pp. 369–374. [Online]. Available: <https://doi.org/10.1145/344779.344951>
- [41] B. Lok, "Online model reconstruction for interactive virtual environments," in *In Proceedings 2001 Symposium on Interactive 3D Graphics*, 2001, pp. 69–72.
- [42] T. Fromherz and M. Bichsel, "Shape From Contours As Initial Step In Shape From Multiple Cues," in *Proceedings of the ISPRS Commission III Symposium on Spatial Information from Digital Photogrammetry and Computer Vision*, 1994, pp. 249–256.
- [43] S. M. Seitz and C. R. Dyer, "Photorealistic Scene Reconstruction by Voxel Coloring," *International Journal of Computer Vision*, vol. 35, no. 2, pp. 151–173, Nov. 1999. [Online]. Available: <https://doi.org/10.1023/A:1008176507526>
- [44] J. Amat, M. Frigola, and A. Casals, "Selection of the best stereo pair in a multi-camera configuration," in *Proceedings 2002 IEEE International Conference on Robotics and Automation (Cat. No.02CH37292)*, vol. 4. Washington, DC, USA: IEEE, 2002, pp. 3342–3346. [Online]. Available: <http://ieeexplore.ieee.org/document/1014227/>
- [45] R. Cipolla, "Projection," University of Cambridge, Oct. 2019. [Online]. Available: <http://mi.eng.cam.ac.uk/~cipolla/lectures/4F12/Slides/2019-4F12-notes-3.pdf>
- [46] S. van der Walt, S. C. Colbert, and G. Varoquaux, "The NumPy Array: A Structure for Efficient Numerical Computation," *Computing in Science & Engineering*, vol. 13, no. 2, pp. 22–30, Mar. 2011. [Online]. Available: <http://ieeexplore.ieee.org/document/5725236/>
- [47] A. De Myttenaere, B. Golden, B. L. Grand, and F. Rossi, "Mean Absolute Percentage Error for regression models," *Neurocomputing*, vol. 192, pp. 38–48, Jun. 2016, arXiv: 1605.02541. [Online]. Available: <http://arxiv.org/abs/1605.02541>
- [48] C. Tofallis, "A Better Measure of Relative Prediction Accuracy for Model Selection and Model Estimation," Social Science Research Network, Rochester, NY, SSRN Scholarly Paper ID 2635088, Jul. 2014. [Online]. Available: <https://papers.ssrn.com/abstract=2635088>
- [49] S. K. Morley, T. V. Brito, and D. T. Welling, "Measures of Model Performance Based On the Log Accuracy Ratio," *Space Weather*, vol. 16, no. 1, pp. 69–88, 2018. [Online]. Available: <https://agupubs.onlinelibrary.wiley.com/doi/abs/10.1002/2017SW001669>



**Eleni Bohacek** graduated with a first class degree in Earth Sciences from University College London (UCL) in 2014, with a specialism in Planetary Science. She then joined the UCL-Cambridge Centre for Doctoral Training in Integrated Photonic and Electronic Systems and completed her MRes in 2015.

She is currently a PhD candidate at the Electronic and Electrical Engineering Department in collaboration with the Mullard Space Science Laboratory at UCL. Her thesis is focused on modelling uncertainty and errors in multi view stereo systems and building an emulator of the European Space Agency 2022 Rosalind Franklin rover camera systems.



**Andrew J. Coates** has been with Mullard Space Science Laboratory, University College London since 1982, with temporary positions at Max Planck Institute for Solar System Physics, Germany, University of Delaware, USA, and BBC World service (media fellowship). He is a Deputy Director (solar system) and Professor of Physics with UCL-MSSL. He is PI of the Rosalind Franklin (ExoMars 2022) PanCam team. He was a co-investigator on instruments for Cassini, Venus Express, Mars Express, and Giotto. He has authored/coauthored more than 525 papers with more than 425 refereed. He received the B.Sc. degree in physics from the University of Manchester Institute of Science and Technology, U.K., in 1978, and the M.Sc. degree and D.Phil. in plasma physics from Oxford University, U.K., in 1979 and 1982, respectively. He is a Fellow of the Royal Astronomical Society and member of the EGU and AGU.



**David R. Selviah** born in England, UK. He received the BA and MA degrees in physics and theoretical physics in 1980 and 1984 respectively and the PhD degree in photonic engineering in 2009 from Trinity College, Cambridge University, Cambridge. UK. He served internships at the Royal Aircraft Establishment, UK, Texas Instruments, UK and CERN, Switzerland. From 1980 to 1983, he was with the Allen Clark Research Center, Plessey (Caswell) Ltd., UK (now Oclaro). From 1983-1986, he was with the Department of Engineering Science, Oxford University, UK. He is currently

a Reader in Optical Devices, Interconnects, Algorithms and Systems in the Optical Devices and Systems Laboratory of the Photonics Research Group in the Electronic and Electrical Engineering Department at University College London, UCL, London. He serves as a consultant to industry and is a founding director of the software company Correvate. He is the author of over 250 published articles, book chapters, keynote conference presentations and patents. His research is generally collaborative with international companies and universities. His current research interests include silicon photonic quantum dot lasers for high bit rate communication in data centers, signal processing, image processing, pattern and 3D object recognition, artificial intelligence, cloud computing, 3D Lidar and photogrammetry, 3D tracking, stimulation and monitoring neural behavior, data analysis for distributed acoustic sensors in oil and gas wells. Dr Selviah is a member of the Institute of Physics, Optical Society of America, European Optical Society and is a Chartered Physicist and Chartered Scientist. He represents the UK on the International Electrotechnical Commission Standards committees IEC TC86, SC86 WG4, SC86 WG6 and JWG9 covering optical fiber connectors, attenuation measurement techniques and optical circuit boards.